ACS APPLIED MATERIALS & INTERFACES

Research Article

www.acsami.org

Tuning the Morphology of g-C_3N_4 for Improvement of Z-Scheme Photocatalytic Water Oxidation

Xiaofei Yang,*[,†,‡] Zupeng Chen,[‡] Jingsan Xu,[‡] Hua Tang,[†] Kangmin Chen,[†] and Yan Jiang[†]

[†]School of Materials Science and Engineering, Jiangsu University, Zhenjiang 212013, China

[‡]Department of Colloid Chemistry, Max Planck Institute of Colloids and Interfaces, Science Park Golm, 14424 Potsdam, Germany

Supporting Information

ABSTRACT: Solar-driven water oxidation is the key step for overall water splitting that efficiently harvests and converts solar energy into fuels; the development of a highly efficient photocatalyst that can mediate water oxidation has become an appealing challenge. Herein, we report a facile two-step process to decorate silver phosphate (Ag_3PO_4) particles on different types of graphitic carbon nitrides (g-C_3N_4) as composite photocatalysts for water oxidation. For all the Ag_3PO_4/g-C_3N_4 materials, an in situ Z-scheme is created by the generation of Ag nanoparticles which act as a cross-linking bridge between Ag_3PO_4 and g-C_3N_4 in the composite, resulting in better charge separation and higher catalytic performance. A detailed analysis emphasizes the importance of the g-C_3N_4 on the chemical, photophysical, and catalytic properties of the composite materials. Our results show that the alteration of the morphology dominates the performance of the composite materials.

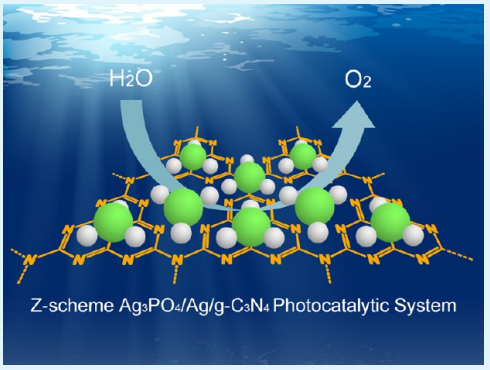

KEYWORDS: *oxygen evolution, water splitting, graphitic carbon nitrides, silver phosphate, Z-scheme, photocatalytic*

INTRODUCTION

Inspired by natural photosynthesis, semiconductor-based photocatalytic water splitting into hydrogen and oxygen has attracted worldwide interest over the past few years.[1−7] In comparison with the two-electron hydrogen evolution reaction (HER), the generation of one molecule of oxygen requires four proton coupled electron transfer. Consequently, the oxygen evolution reaction (OER) results in a large overpotential due to the high kinetic barrier compared to hydrogen evolution. For an efficient photocatalyst several requirements should be fulfilled: (1) good light-harvesting properties; (2) a suitable band gap and energy bands position for the desired reaction; (3) good photostability and chemical stability. Although significant recent advances have been made in the development of photocatalysts for hydrogen evolution from water,[8−12] by far only a few photocatalysts have been proven to be efficient for visible-light-driven oxygen evolution from water.[13−15]

A promising photocatalyst for oxygen evolution is silver phosphate (Ag_3PO_4) due to its strong photo-oxidative properties.[16,17] However, there are several drawbacks that limit its practical application in oxygen-generating photocatalytic systems, including poor photostability, high costs of raw materials, and difficulties in implementing size and morphology control. Recently, efforts have been made to overcome these problems by the development of new Ag_3PO_4-based composite photocatalysts (with different semiconductors) with enhanced light-harvesting ability, faster charge separation and transfer, and improved photocatalytic activity.[18−27] However, the application of Ag_3PO_4-based composite materials has been mainly focused on the photodegradation of organic pollutants via the conventional heterojunction mechanism, where photogenerated electrons are accumulated into the conduction band (CB) of Ag_3PO_4 while the holes transfer to the VB of the complementary semiconductor. The development of Ag_3PO_4-based composite materials for specific Z-scheme applications, in particular water oxidation, is still a challenge. For an efficient OER photocatalyst, an opposite charge transfer is desired in which the holes stay in the VB of the Ag_3PO_4, while the destabilizing electrons (Ag_3PO_4 is self-photoreductive) should be removed.

Graphitic carbon nitride (g-C_3N_4) has drawn immense attention due to its robust nature and special electronic band structure.[28−35] Intensive studies focused on synthesizing new g-C_3N_4-based photocatalysts and investigating their hydrogen evolution from water.[8,36−42] The g-C_3N_4/Ag_3PO_4 composite has been suggested as an efficient photocatalyst for CO_2 reduction[43] and dye degradation.[44−46] Very recently, for the first time, we showed that the g-C_3N_4/Ag_3PO_4 composite demonstrates high activity for oxygen production.[47] Experimental evidence indicates that the enhancement in stability and activity ascribes to the formation of in situ Z-scheme under illumination which improves the charge separation within the composite. In order to further understand the structure−property relationship of the g-C_3N_4/Ag_3PO_4 composite in photocatalytic water oxidation, herein we aim to study the influence of the variation of g-C_3N_4 materials, as well as the

Received: April 10, 2015
Accepted: June 28, 2015
Published: June 29, 2015

DOI: 10.1021/acsami.5b02649
ACS Appl. Mater. Interfaces 2015, 7, 15285−15293

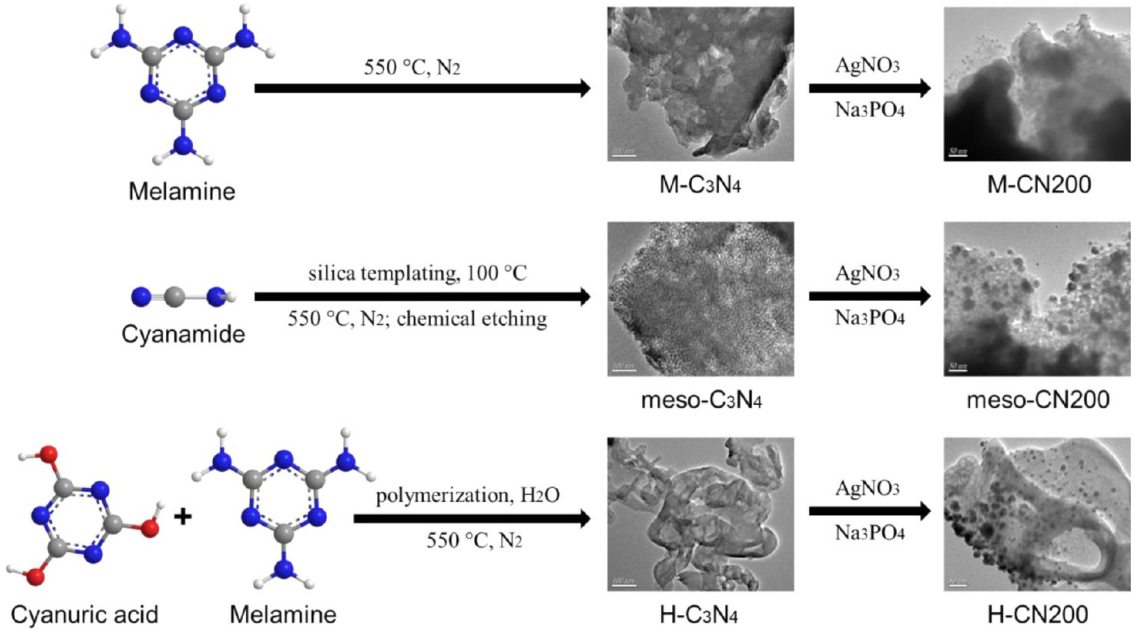

Figure 1. Schematic illustration of the synthesis of g-C_3N_4 samples and the corresponding Ag_3PO_4/g-C_3N_4 composites.

interface contact between two different semiconductors, on the physicochemical properties and oxygen evolution performance of the g-C_3N_4/Ag_3PO_4 composite. The Ag_3PO_4/g-C_3N_4 composites were synthesized via electrostatic assembly and solution-based precipitation in a two-step procedure. For all the Ag_3PO_4/g-C_3N_4 composite photocatalysts, in situ photoreduced Ag nanoparticles may act as the recombination center for electrons and holes from different materials, forming a more efficient Z-scheme photocatalytic oxygen-evolving system. The photocatalytic properties were tested by measuring the O_2 evolution which clearly underlined the importance of the electronic and chemical properties of the selected g-C_3N_4 on the photocatalytic water oxidation.

EXPERIMENTAL SECTION

Synthesis of C_3N_4 Samples. All chemicals were of analytical grade and used as received without further purification. Modified graphitic carbon nitrides were synthesized by using equimolar amounts of cyanuric acid and melamine according to our previous papers.[47] In a typical synthesis, cyanuric acid (10 mmol, 1.29 g) and melamine (10 mmol, 1.26 g) were first ground gently and then mixed in water with stirring for 8 h. The obtained cyanuric acid−melamine (CM) complexes were collected by centrifugation and dried in vacuum. As-prepared white CM complexes powder was subsequently calcined at 550 °C under N_2 for 4 h with the heating rate of 2.3 °C min^{-1}, and the calcined light yellow powder is denoted as H-C_3N_4. The bulk graphitic C_3N_4 was synthesized as a reference sample by directly placing 2 g of melamine in a crucible and calcining at 550 °C under N_2 for 4 h; the sample is denoted as M-C_3N_4 while the same annealing conditions were employed for the preparation of H-C_3N_4.

Mesoporous graphitic carbon nitrides (meso-C_3N_4) were prepared by directly dispersing 1.25 g cyanamide in water, followed by the addition of 12 nm colloidal silica with stirring at 100 °C overnight to remove water. The weight ratio between precursors and silica was always kept as 1:1. The resultant white powder was ground gently and then calcined at 550 °C under the same thermal conditions. The obtained brown-yellow powders were washed repeatedly with 4 M NH_4HF_2 solution to remove the silica template. Afterward, the powders were filtered, and washed repeatedly with water and absolute ethanol until neutral. Finally the products were dried at 60 °C under vacuum overnight.

Synthesis of Ag_3PO_4/g-C_3N_4 Composites. The corresponding Ag_3PO_4/g-C_3N_4 composites were synthesized by combining electrostatically driven assembly of Ag^+ and g-C_3N_4 with solution ion-exchange process. In a typical synthesis, different g-C_3N_4 (200 mg) samples were first ultrasonicated in deionized water (50 mL) to give g-C_3N_4 aqueous dispersions. Subsequently, 30 mL of $AgNO_3$ (0.3 M) aqueous solution was added slowly into the corresponding g-C_3N_4 dispersion. After the addition, the obtained mixture was stirred gently overnight to promote the assembly of positively charged Ag^+ on the surface of negatively charged g-C_3N_4. Finally, the addition of Na_3PO_4 aqueous solution (0.1 M, 30 mL) dropwise into the above Ag^+/g-C_3N_4 mixture resulted in the generation of yellow green precipitates. The obtained precipitates were then centrifuged, washed repeatedly with deionized water and absolute ethanol, and finally dried at 60 °C in vacuum to yield three kinds of Ag_3PO_4/g-C_3N_4 samples. The Ag_3PO_4/C_3N_4 composites with 200 mg M-C_3N_4, meso-C_3N_4, and H-C_3N_4 were denoted as M-CN200, meso-CN200, and H-CN200, respectively.

Characterization. The morphological features of the obtained materials were evaluated by field-emission scanning electron microscopy (FE-SEM, JSM-7001F) and transmission electron microscopy (TEM, JEM-2100). The crystal structures of the composites were determined on a Bruker D8 Advance diffractometer using Cu Kα1 radiation (λ = 1.5406 Å). Fourier transform infrared spectra (FT-IR) of as-prepared samples were collected using a Thermo Scientific Nicolet is5 FTIR spectrometer (ATR-Diamond mode). The UV−vis diffuse reflectance spectra of different materials were measured on a SHIMADZU UV-2600 spectrophotometer. The chemical states and species were studied by using X-ray photoelectron spectroscopy (XPS, Perkin−Elmer PHI 5000C). Nitrogen sorption characterizations were conducted on a Quantachrome Quadrasorb SI porosimeter under N_2 at 77 K after 15 h degassing at 150 °C. The Brunauer−Emmett−Teller (BET) model was applied to the calculation of surface areas of different materials on the basis of the isotherm data points of the adsorption branch. ESR measurements were also carried out on a Bruker A300 Spectrometer.

Photocatalytic Oxygen Evolution. The efficiency of photocatalytic O_2 evolution was determined by a highly sensitive oxygen probe (PreSens Precision Sensing GmbH) in a sealed system, where a double-layered flask was used and connected to a water-cooling pump. Before the measurement, standard calibration solutions (0% and 100%) were employed in order to calibrate the optical fiber oxygen probe with temperature compensation. Under illumination, the temperature of the reactor can be kept at room temperature due to

DOI: 10.1021/acsami.5b02649
ACS Appl. Mater. Interfaces 2015, 7, 15285−15293

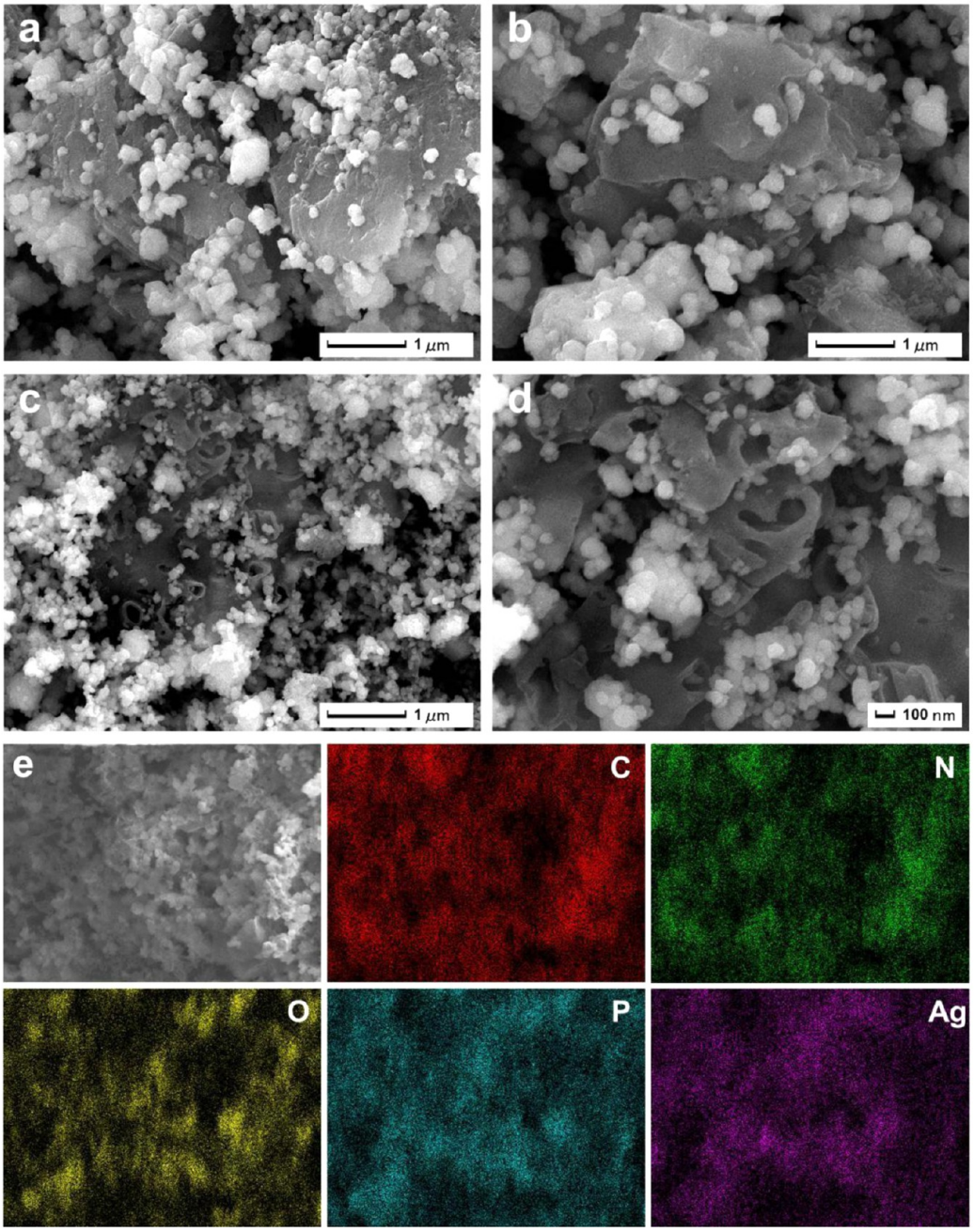

Figure 2. SEM images of (a) M-CN200, (b) meso-CN200, and (c, d) H-CN200, and (e) elemental mapping results of the $Ag_3PO_4/g\text{-}C_3N_4$ composite H-CN200.

the presence of the water-cooling system. Additionally, the oxygen probe is temperature-compensated and is connected to a sensitive temperature probe, indicating that oxygen-generating efficiency from water splitting can be determined in a good manner. For a typical oxygen evolution experiment, the photocatalyst powder (0.3 g) was dispersed and mixed with $AgNO_3$ aqueous solution (100 mL 10 g/L). The mixture was then stirred in dark to reach the equilibrium before the illumination under an LED white light source. The distance between the white LED light and the reactor was 10 cm. The photocatalytic oxygen-producing activities over three catalysts were evaluated by measuring the O_2 generated under regular time intervals. Moreover, several experiments including blank sample under light illumination, blank sample under dark condition, and the irradiated catalyst without the sacrificial agent $AgNO_3$ were carried out for comparisons.

RESULTS AND DISCUSSION

$Ag_3PO_4/g\text{-}C_3N_4$ composites were synthesized by a two-step process as shown in Figure 1. In this study, three different C_3N_4, (1) M-C_3N_4, (2) meso-C_3N_4, and (3) H-C_3N_4, were used as the precursors for the preparation of $Ag_3PO_4/g\text{-}C_3N_4$ composites. The obtained g-C_3N_4 was first ultrasonicated to give exfoliated g-C_3N_4 dispersions. Afterward, $AgNO_3$ aqueous solution was added, and the materials were slowly stirred overnight resulting in electrostatically driven assembly of Ag^+ on g-C_3N_4 surface. The $Ag^+/g\text{-}C_3N_4$ intermediates were subsequently converted to Ag_3PO_4/C_3N_4 by adding the precipitant, Na_3PO_4.

Morphological, Compositional, and Structural Studies. The morphologies of g-C_3N_{4s}, Ag_3PO_4, and $Ag_3PO_4/g\text{-}$

DOI: 10.1021/acsami.5b02649
ACS Appl. Mater. Interfaces 2015, 7, 15285−15293

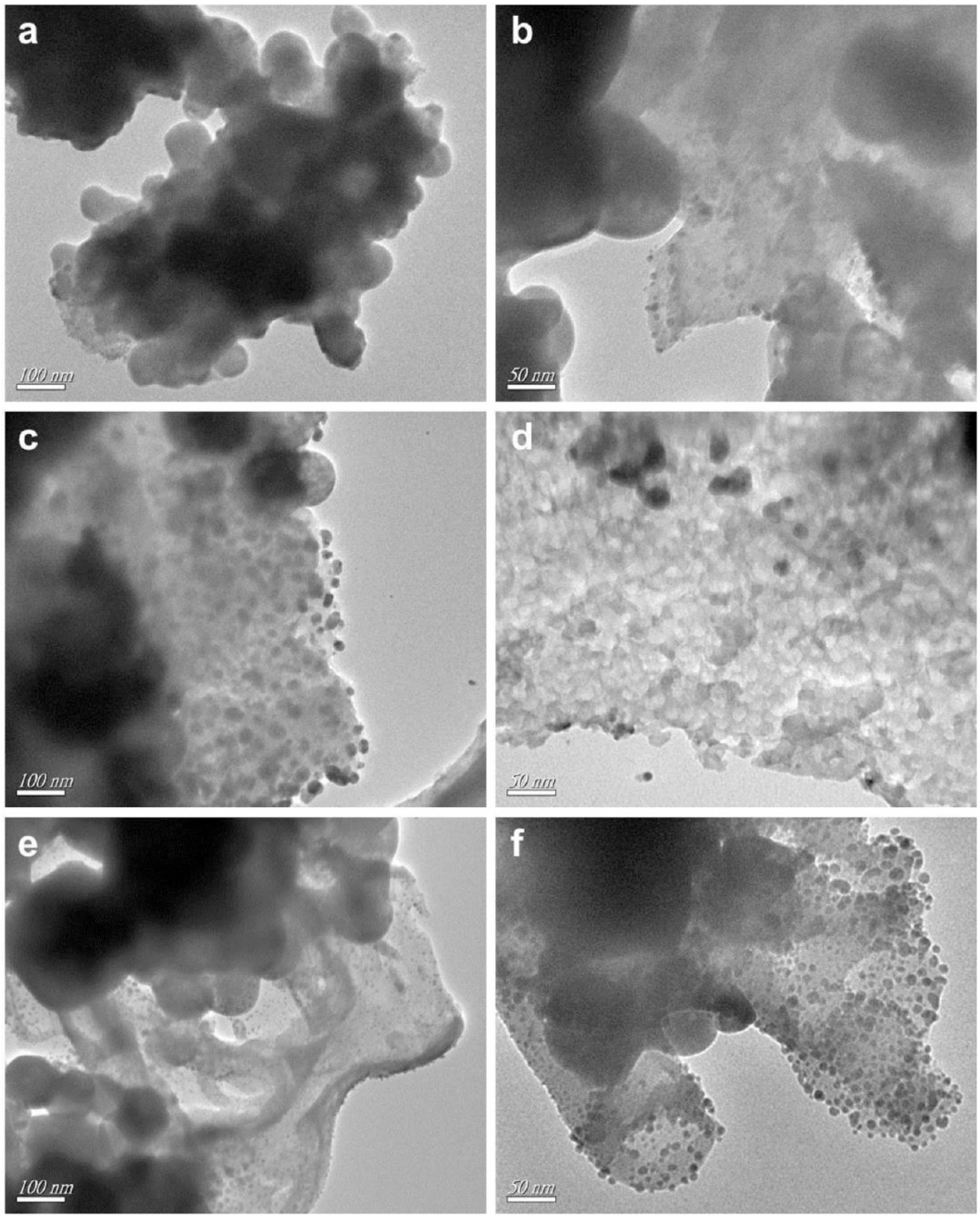

Figure 3. TEM images of M-CN200 (a, b), meso-CN200 (c, d), and H-CN200 (e, f).

C_3N_4 composites were investigated by FE-SEM and TEM (Supporting Information Figure S1). The C_3N_4 from direct melamine condensation showed a bulk-like morphology (Supporting Information Figure S1a) with only a few sheets on the surface while for the templated one a mesoporous structure was observed (Supporting Information Figure S1b, meso-C_3N_4). The H-C_3N_4 obtained from the calcination of the cyanuric acid−melamine complex in water exhibited a rough surface consisting of interconnected and curved g-C_3N_4 sheets with porous structure (Supporting Information Figure S1c). Figure 2 shows FE-SEM images of different Ag_3PO_4/g-C_3N_4 composites derived from 200 mg of g-C_3N_4 and 3 mmol of Ag_3PO_4. It is shown in Figure 2a that microsized Ag_3PO_4 particles are poorly and randomly deposited on exfoliated M-C_3N_4 sheets in the composite M-CN200. For the composite (Figure 2b) made from meso-C_3N_4, larger Ag_3PO_4 particles were observed on its surface. However, smaller Ag_3PO_4 nanoparticle-decorated porous and thin g-C_3N_4 sheets were detected in the H-CN200 composite (Figure 2c). High-magnification FE-SEM image (Figure 2d) further reveals the hybridization of nanosized Ag_3PO_4 with porous H-C_3N_4 sheets. Compared with bulk Ag_3PO_4 (Supporting Information Figure S2), the size of Ag_3PO_4 particles in all composites is smaller, implying that the presence of g-C_3N_4 in the composite may effectively tune the size of Ag_3PO_4 particles. Moreover, the Ag_3PO_4 nanoparticles in the composite H-CN200 are more uniform and smaller than those in the composites M-CN200 and meso-CN200, indicating the importance of the appropriate carbon nitride species on the growth of Ag_3PO_4 particles. EDX (Supporting Information Figure S3) spectra confirm the

DOI: 10.1021/acsami.5b02649
ACS Appl. Mater. Interfaces 2015, 7, 15285−15293

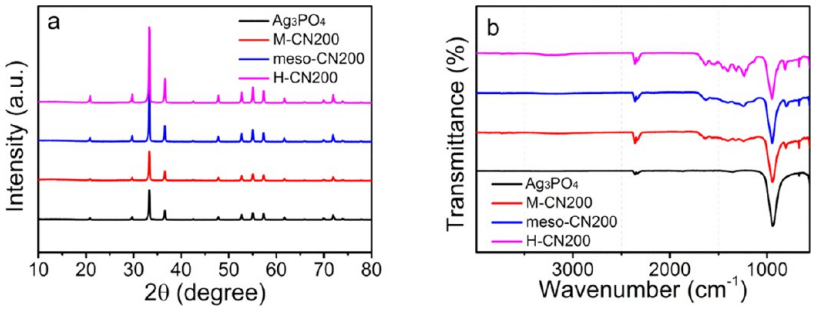

Figure 4. XRD patterns (a) and ATR-FTIR spectra (b) of Ag_3PO_4 and Ag_3PO_4/g-C_3N_4 composites.

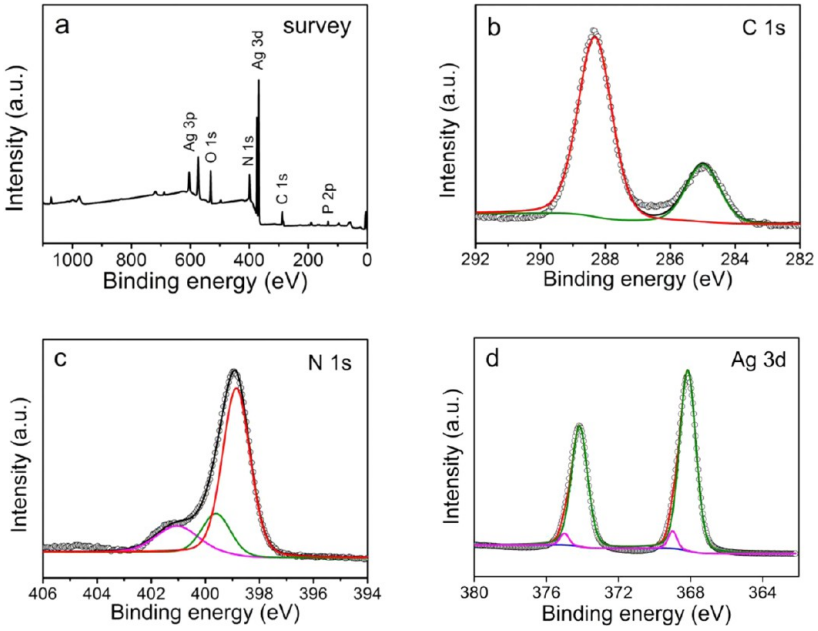

Figure 5. XPS survey (a), and high-resolution (b) C1 s, (c) N 1s, and (d) Ag 3d spectra of the Ag_3PO_4/g-C_3N_4 composite H-CN200.

presence of C, N, O, P, Ag elements in the composite H-CN200, and elemental mapping results (Figure 2e) further verify the homogeneous distribution of different elements in the composite H-CN200.

Additionally, TEM characterization was used in order to further clarify the morphological differences in the Ag_3PO_4/g-C_3N_4 composites (Figure 3). The importance of C_3N_4 morphology is clearly evident from the TEM images of the composite materials. Only for the composite H-CN200 was a homogeneous deposition of Ag_3PO_4 particles achieved (Figure 3c), while for the composites derived from mesoporous (Figure 3b) and bulk (Figure 3a) g-C_3N_4, a poor hybridization was observed. It is also notable that, for all Ag_3PO_4/g-C_3N_4 composites, nearly all Ag_3PO_4 particles were deposited on the matrix g-C_3N_4, indicating the preferred nucleation of this species by a supportive tight interfacial contact.

The crystal structure of all the materials was determined by XRD (Figure 4a). All three composites exhibited similar patterns to that of the body-centered cubic Ag_3PO_4 (JCPDS 06-0505). However, the g-C_3N_4 was not observed due to its low amount and the high crystallinity of Ag_3PO_4. The presence of g-C_3N_4 in the composite was confirmed by the ATR-FTIR measurements. For all g-C_3N_4 samples (Supporting Information Figure S4), several bands ranging from 1200 to 1650 cm^{-1} were observed. Peaks around 1235, 1315, 1402, 1550, and 1630 cm^{-1} are suggested to originate from the characteristic stretching modes of CN heterocycles, while the peak at 810 cm^{-1} is assigned to the typical breathing mode of triazine units. No obvious difference in ATR-FTIR spectra was detected for all the obtained samples. Additionally, characteristic P−O stretching modes (946−950 and 668 cm^{-1}) were observed in all the composites. In comparison with the typical bands (941 and 668 cm^{-1}) in bulk Ag_3PO_4, the corresponding P−O stretching mode at 941 cm^{-1} in bulk Ag_3PO_4 depicted a slight shift to the higher wavenumbers of 946, 949, and 950 cm^{-1} in composites M-CN200, meso-CN200, and H-CN200, respectively. The phenomenon implies that in this method the materials have strong interactions and are not just physically mixed.

The surface chemical compositions and elemental binding state were examined by XPS, and for simplicity only the XPS results of the most efficient H-CN200 are shown (Figure 5). The XPS survey spectrum of the composite H-CN200 shows the presence of C, N, O, P, and Ag (Figure 5a). The high-resolution C 1s spectrum (Figure 5b) can be fitted into two main peaks at 284.8 and 288.4 eV, which correspond to sp^2 carbon species in a purely carbonaceous environment and sp^2-bonded carbon atoms in N-containing aromatic rings. Moreover, the corresponding high-resolution N 1s spectrum can be deconvoluted into three different nitrogen species (Figure 5c), namely, the aromatic nitrogen atom bonded to two different carbon atoms (C═N—C, 398.8 eV), the tertiary N groups

DOI: 10.1021/acsami.5b02649
ACS Appl. Mater. Interfaces 2015, 7, 15285−15293

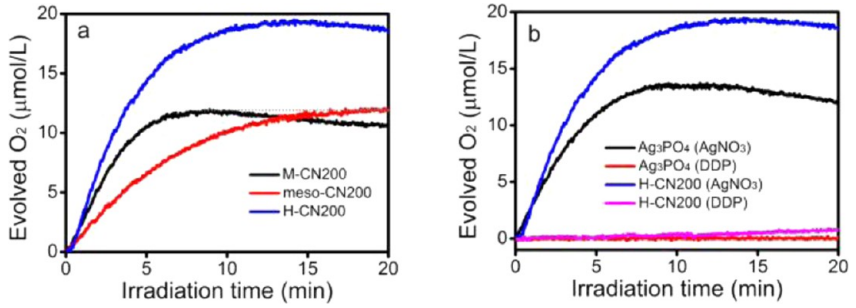

Figure 6. Visible-light-driven oxygen evolution activity over (a) different Ag_3PO_4/g-C_3N_4 composites, and (b) the composite H-CN200 and Ag_3PO_4 in the presence of $AgNO_3$ and DDP.

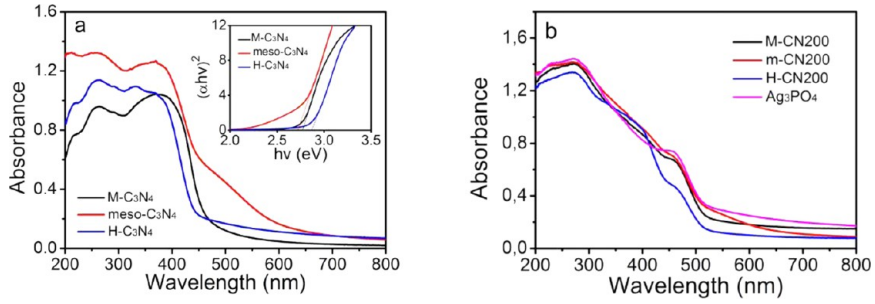

Figure 7. UV−vis diffuse reflectance spectra of (a) different g-C_3N_4, (b) bulk Ag_3PO_4, and the Ag_3PO_4/g-C_3N_4 composites.

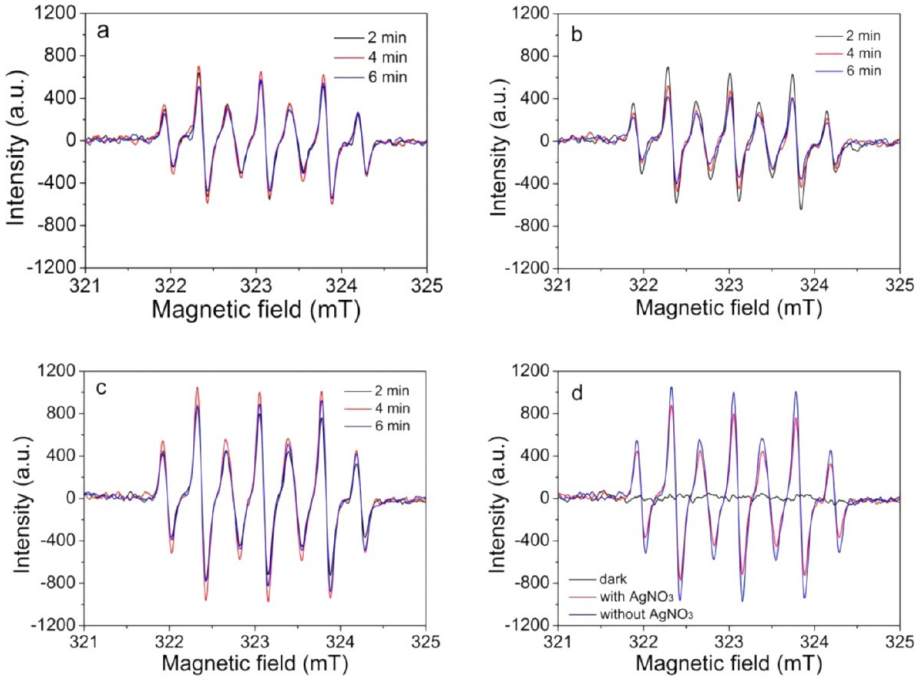

Figure 8. DMPO-$^{\bullet}$OH adducts of (a) M-CN200, (b) meso-CN200, (c) H-CN200 under visible light irradiation in the presence of $AgNO_3$, and (d) the selected Ag_3PO_4/g-C_3N_4 composite H-CN200 under different conditions.

(N—(C)$_3$, 399.7 eV), and the terminal amino functional groups (C—N—H, 401.1 eV). All the results indicate the existence of the heptazine heterocyclic ring (C_6N_7) units, which are the elementary building blocks of g-C_3N_4. Two distinct peaks at 368.2 eV (Ag $3d_{5/2}$) and 374.2 eV (Ag $3d_{3/2}$) were also detected in the high-resolution Ag 3d spectrum (Figure 5d) of H-CN200, which corresponds to the metallic Ag in the composite. The Ag $3d_{5/2}$ peak can be further deconvoluted into two peaks at 368.2 and 369.0 eV, while the Ag $3d_{3/2}$ peak can be divided into two peaks at 374.2 and 375.0 eV, respectively. Intense peaks of 368.2 and 374.2 eV are attributed to Ag^+ while the peaks of 369.0 and 375.0 eV are assigned to metallic Ag (Ag^0).

Oxygen Evolution Performance and Possible Mechanism. The photocatalytic performance for oxygen evolution of the different Ag_3PO_4/g-C_3N_4 materials was studied by employing $AgNO_3$ as the sacrificial agent (Figure 6a). The H-C_3N_4 exhibited the fastest reaction rate and the highest

DOI: 10.1021/acsami.5b02649
ACS Appl. Mater. Interfaces 2015, 7, 15285−15293

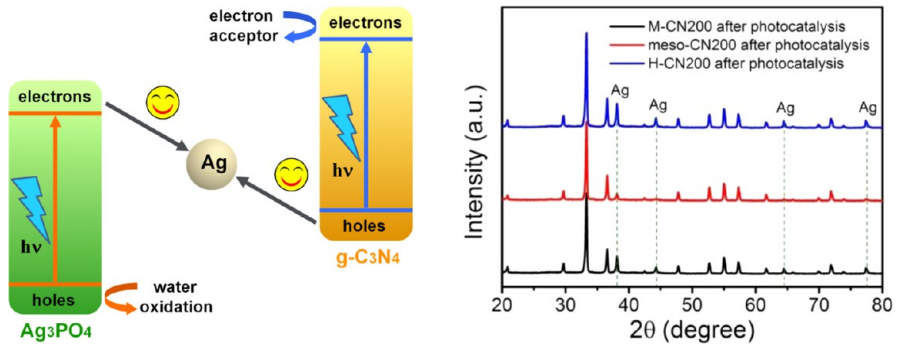

Figure 9. (Left) Schematic illustration for the charge separation and transfer in solar-driven Z-scheme $Ag_3PO_4/Ag/g\text{-}C_3N_4$ ternary photocatalytic system. (Right) XRD patterns of the $Ag_3PO_4/g\text{-}C_3N_4$ composites after photocatalysis.

amount of oxygen production (~20 μmol/L). For the bulk and mesoporous C_3N_4 the final oxygen amount was similar, but the reaction rate was faster for the M-C_3N_4 system. The effect of g-C_3N_4 on the total performance is demonstrated in the additional oxygen evolution for only H-CN200 compared to bulk Ag_3PO_4 (Figure 6b). The changes in the reaction rates and the total oxygen production can be due to the various morphologies which result in different chemical, electronic, and catalytic properties.

Moreover, in order to understand the role of $AgNO_3$, a platinum-based chemical diamminedinitritoplatinum (DDP) was also employed as an electron trap. It is shown from Figure 6b that, in the presence of $AgNO_3$, both bulk Ag_3PO_4 and the composite H-CN200 produced specific amounts of O_2. The evolved O_2 efficiency over Ag_3PO_4 was 13 μmol/L in 10 min followed by a slight decay to 11 μmol/L in 20 min, while H-CN200 revealed a better oxygen activity of 19 μmol/L in 14 min without obvious decrease when prolonged to 20 min. However, when $AgNO_3$ was replaced by the electron trap DDP, both samples showed a negligible oxygen-producing activity, suggesting the key role of $AgNO_3$ in the irradiated $Ag_3PO_4/g\text{-}C_3N_4$ water splitting system.

The optical properties of g-C_3N_4, $Ag_3PO_4/g\text{-}C_3N_4$ composites were studied by UV−vis diffuse reflectance spectroscopy (DRS) and are shown in Figure 7. The threshold of M-C_3N_4 was located at approximately 460 nm, while modified H-C_3N_4 exhibited a slight blue-shift of the edge (450 nm) because of the size confinement effect. For meso-C_3N_4, a significant enhancement in the absorbance alongside a clear red-shift was observed, due to the templating process which improves the light-harvesting ability. The band gap values of the corresponding M-C_3N_4, meso-C_3N_4, and H-C_3N_4 are determined to be around 2.74, 2.68, and 2.87 eV, respectively (Figure 7a, inset). The loading of Ag_3PO_4 into g-C_3N_4 further enhances its light absorption and results in an obvious red-shift in the absorption edge up to 550 nm (Figure 7b).

In order to reveal the mechanism behind the oxygen evolution, active radicals involved in the oxygen-evolving process were investigated by ESR in situ characterizations of the illuminated $Ag_3PO_4/g\text{-}C_3N_4$ composites with 5,5-dimethyl-1-pyrroline-*N*-oxide (DMPO) in water and methanol, respectively. Comparative ESR signals for DMPO-$^{\bullet}$OH adducts in illuminated composite photocatalysts were recorded (Figure 8). It is shown in Figure 8a that seven characteristic peaks from 5,5-dimethyl-2-ketopyrrolidino-1-oxyl (DMPOX) appear. DMPOX is a derivative of DMPO and is believed to come from further interactions between active hydroxyl species and the obtained DMPO-$^{\bullet}$OH adducts. The DMPOX production in the presence of $AgNO_3$ is maximized after 4 min for M-CN200 and (Figure 8a) after 2 min for meso-CN200 (Figure 8b), whereas both exhibited a similar maximum intensity (less than 800). A higher intensity (more than 1100) was observed for the illuminated H-CN200 (Figure 8c), due to faster charge separation and transfer. Additionally, no ESR signal was detected in the dark, which confirms that illumination is of great importance to the formation of active oxygen-containing radicals. Furthermore, in the absence of $AgNO_3$, typical signals from DMPOX under 2 min irradiation were recorded for the H-C_3N_4, suggesting that more hydroxyl radicals were generated due to the reduction of oxygen.

On the basis of the above results and discussion, the photocatalytic mechanism for OER is proposed (Figure 9, left). Unlike the conventional mechanism for a two-phase heterojunctions, under illumination, the generated metallic Ag immediately constructs a cross-linking bridge for two semiconductors. The recombination of electrons from the CB of Ag_3PO_4 and holes from the VB of g-C_3N_4 on Ag surface may strongly increase the electron−hole lifetime in each material. The remaining holes on the CB of Ag_3PO_4 can effectively oxidize water, while the electrons in the CB of g-C_3N_4 may reduce $AgNO_3$. Additionally, there are several factors that influence the photocatalytic activity: (1) particle size and the morphology, (2) interfacial contact area, and (3) light-harvesting ability. Our study shows that the composite H-CN200 is the most efficient OER catalyst despite the lower and blue-shifted visible light absorption. The phenomenon can be explained by the variations in the as-prepared g-C_3N_4 and the interfacial contact between Ag_3PO_4 and g-C_3N_4. As evidenced in Supporting Information Figure S1, H-C_3N_4 morphology is more uniform compared to those of M-C_3N_4 and meso-C_3N_4. Furthermore, Ag_3PO_4 particles are relatively smaller and better distributed in H-C_3N_4 compared to M-C_3N_4 and meso-C_3N_4. A larger surface area (26.1 m^2/g) was also observed for H-CN200 in comparison with M-CN200 (6.0 m^2/g) and meso-CN200 (17.0 m^2/g). It is suggested that a higher surface area may provide more active sites for OER. In addition, XRD results of the composites after photocatalysis (Figure 9, right) reveal that a higher percentage of Ag is generated in H-CN200 than those in illuminated M-CN200 and meso-CN200, suggesting more efficient charge transport and faster water oxidation.

CONCLUSIONS

In summary, we report the fabrication of different g-C_3N_4/Ag_3PO_4 composite materials and their photoactivity for the oxygen evolution reaction. The activity of Ag_3PO_4 can be tuned

DOI: 10.1021/acsami.5b02649
ACS Appl. Mater. Interfaces 2015, 7, 15285−15293

through the incorporation of modified g-C_3N_4 by the formation of Ag_3PO_4/Ag/g-C_3N_4 Z-scheme under illumination. The in situ generated metallic Ag acts as the recombination center of photogenerated electrons from Ag_3PO_4 and holes from g-C_3N_4, keeping the active holes on the VB of Ag_3PO_4 for water oxidation. This study emphasizes the importance of the chemical and electronic properties of the supporting C_3N_4 structure for efficient OER catalyst. The fabrication of the Ag_3PO_4/g-C_3N_4 composites can be extended to the design of a variety of g-C_3N_4-based composite photocatalytic materials for energy and environmental applications.

■ ASSOCIATED CONTENT

Supporting Information

FE-SEM and TEM images of g-C_3N_4 samples, FE-SEM images of bulk Ag_3PO_4, EDX spectra of the Ag_3PO_4/g-C_3N_4 composite H-CN200, and ATR-FTIR spectra of different g-C_3N_4 samples. The Supporting Information is available free of charge on the ACS Publications website at DOI: 10.1021/acsami.5b02649.

■ AUTHOR INFORMATION

Corresponding Author

*E-mail: Xiaofei.Yang@mpikg.mpg.de.

Notes

The authors declare no competing financial interest.

■ ACKNOWLEDGMENTS

X.Y. gratefully acknowledges financial support from the Max Planck Society via a fellowship. This work was also financially supported by the National Natural Science Foundation of China (51102116, 51302112), Natural Science Foundation of Jiangsu (BK2011480), Jiangsu Overseas Research & Training Program for University Prominent Young & Middle-Aged Teachers, the Specialized Research Fund for Cultivating Academic Leader of Jiangsu University, China, and Open Fund of Key Laboratory for Intelligent Nano Materials and Devices of the Ministry of Education (INMD-2014M02).

■ REFERENCES

(1) Ran, J. R.; Zhang, J.; Yu, J. G.; Jaroniec, M.; Qiao, S. Z. Earth-Abundant Cocatalysts for Semiconductor-Based Photocatalytic Water Splitting. *Chem. Soc. Rev.* **2014**, *43*, 7787−7812.

(2) Liu, C.; Dasgupta, N. P.; Yang, P. D. Semiconductor Nanowires for Artificial Photosynthesis. *Chem. Mater.* **2014**, *26*, 415−422.

(3) Liu, B.; Wu, C. H.; Miao, J. W.; Yang, P. D. All Inorganic Semiconductor Nanowire Mesh for Direct Solar Water Splitting. *ACS Nano* **2014**, *8*, 11739−11744.

(4) Liu, C.; Tang, J. Y.; Chen, H. M.; Liu, B.; Yang, P. D. A Fully Integrated Nanosystem of Semiconductor Nanowires for Direct Solar Water Splitting. *Nano Lett.* **2013**, *13*, 2989−2992.

(5) Hisatomi, T.; Kubota, J.; Domen, K. Recent Advances in Semiconductors for Photocatalytic and Photoelectrochemical Water Splitting. *Chem. Soc. Rev.* **2014**, *43*, 7520−7535.

(6) Moriya, Y.; Takata, T.; Domen, K. Recent Progress in the Development of (Oxy)nitride Photocatalysts for Water Splitting under Visible-Light Irradiation. *Coord. Chem. Rev.* **2013**, *257*, 1957−1969.

(7) Takanabe, K.; Domen, K. Preparation of Inorganic Photocatalytic Materials for Overall Water Splitting. *ChemCatChem* **2012**, *4*, 1485−1497.

(8) Cao, S. W.; Yu, J. G. g-C_3N_4-Based Photocatalysts for Hydrogen Generation. *J. Phys. Chem. Lett.* **2014**, *5*, 2101−2107.

(9) Zhang, J. Y.; Wang, Y. H.; Zhang, J.; Lin, Z.; Huang, F.; Yu, J. G. Enhanced Photocatalytic Hydrogen Production Activities of Au-Loaded ZnS Flowers. *ACS Appl. Mater. Interfaces* **2013**, *5*, 1031−1037.

(10) Zhang, J. Y.; Wang, Y. H.; Jin, J.; Zhang, J.; Lin, Z.; Huang, F.; Yu, J. G. Efficient Visible-Light Photocatalytic Hydrogen Evolution and Enhanced Photostability of Core/Shell CdS/g-C_3N_4 Nanowires. *ACS Appl. Mater. Interfaces* **2013**, *5*, 10317−10324.

(11) Xiang, Q. J.; Yu, J. G. Graphene-Based Photocatalysts for Hydrogen Generation. *J. Phys. Chem. Lett.* **2013**, *4*, 753−759.

(12) Xiang, Q. J.; Yu, J. G.; Jaroniec, M. Synergetic Effect of MoS_2 and Graphene as Cocatalysts for Enhanced Photocatalytic H_2 Production Activity of TiO_2 Nanoparticles. *J. Am. Chem. Soc.* **2012**, *134*, 6575−6578.

(13) Xie, Y. P.; Liu, G.; Lu, G. Q.; Cheng, H. M. Boron Oxynitride Nanoclusters on Tungsten Trioxide as a Metal-Free Cocatalyst for Photocatalytic Oxygen Evolution from Water Splitting. *Nanoscale* **2012**, *4*, 1267−1270.

(14) Hou, Y.; Zuo, F.; Ma, Q.; Wang, C.; Bartels, L.; Feng, P. Y. Ag_3PO_4 Oxygen Evolution Photocatalyst Employing Synergistic Action of Ag/AgBr Nanoparticles and Graphene Sheets. *J. Phys. Chem. C* **2012**, *116*, 20132−20139.

(15) Kho, Y. K.; Teoh, W. Y.; Iwase, A.; Madler, L.; Kudo, A.; Amal, R. Flame Preparation of Visible-Light-Responsive $BiVO_4$ Oxygen Evolution Photocatalysts with Subsequent Activation via Aqueous Route. *ACS Appl. Mater. Interfaces* **2011**, *3*, 1997−2004.

(16) Yi, Z. G.; Ye, J. H.; Kikugawa, N.; Kako, T.; Ouyang, S. X.; Stuart-Williams, H.; Yang, H.; Cao, J. Y.; Luo, W. J.; Li, Z. S.; Liu, Y.; Withers, R. L. An Orthophosphate Semiconductor with Photooxidation Properties under Visible-Light Irradiation. *Nat. Mater.* **2010**, *9*, 559−564.

(17) Bi, Y.; Ouyang, S.; Umezawa, N.; Cao, J.; Ye, J. Facet Effect of Single-Crystalline Ag_3PO_4 Sub-microcrystals on Photocatalytic Properties. *J. Am. Chem. Soc.* **2011**, *133*, 6490−6492.

(18) Yang, X. F.; Qin, J. L.; Jiang, Y.; Li, R.; Li, Y.; Tang, H. Bifunctional TiO_2/Ag_3PO_4/ Graphene Composites with Superior Visible Light Photocatalytic Performance and Synergistic Inactivation of Bacteria. *RSC Adv.* **2014**, *4*, 18627−18636.

(19) Yang, X. F.; Cui, H. Y.; Li, Y.; Qin, J. L.; Zhang, R. X.; Tang, H. Fabrication of Ag_3PO_4-Graphene Composites with Highly Efficient and Stable Visible Light Photocatalytic Performance. *ACS Catal.* **2013**, *3*, 363−369.

(20) Cui, H. Y.; Yang, X. F.; Gao, Q. X.; Liu, H.; Li, Y.; Tang, H.; Zhang, R. X.; Qin, J. L.; Yan, X. H. Facile Synthesis of Graphene Oxide-Enwrapped Ag_3PO_4 Composites with Highly Efficient Visible Light Photocatalytic Performance. *Mater. Lett.* **2013**, *93*, 28−31.

(21) Xiang, Q. J.; Lang, D.; Shen, T. T.; Liu, F. Graphene-Modified Nanosized Ag_3PO_4 Photocatalysts for Enhanced Visible-Light Photocatalytic Activity and Stability. *Appl. Catal., B* **2015**, *162*, 196−203.

(22) Cui, C.; Wang, Y. P.; Liang, D. Y.; Cui, W.; Hu, H. H.; Lu, B. Q.; Xu, S.; Li, X. Y.; Wang, C.; Yang, Y. Photo-Assisted Synthesis of Ag_3PO_4/Reduced Graphene Oxide/Ag Heterostructure Photocatalyst with Enhanced Photocatalytic Activity and Stability under Visible Light. *Appl. Catal., B* **2014**, *158*, 150−160.

(23) Xu, J. W.; Gao, Z. D.; Han, K.; Liu, Y. M.; Song, Y. Y. Synthesis of Magnetically Separable Ag_3PO_4/TiO_2/Fe_3O_4 Heterostructure with Enhanced Photocatalytic Performance under Visible Light for Photoinactivation of Bacteria. *ACS Appl. Mater. Interfaces* **2014**, *6*, 15122−15131.

(24) Guan, X. J.; Guo, L. J. Cocatalytic Effect of $SrTiO_3$ on Ag_3PO_4 toward Enhanced Photocatalytic Water Oxidation. *ACS Catal.* **2014**, *4*, 3020−3026.

(25) Peng, W. C.; Wang, X.; Li, X. Y. The Synergetic Effect of MoS_2 and Graphene on Ag_3PO_4 for Its Ultra-Enhanced Photocatalytic Activity in Phenol Degradation under Visible Light. *Nanoscale* **2014**, *6*, 8311−8317.

(26) Yang, Z. M.; Huang, G. F.; Huang, W. Q.; Wei, J. M.; Yan, X. G.; Liu, Y. Y.; Jiao, C.; Wan, Z.; Pan, A. L. Novel Ag_3PO_4/CeO_2 Composite with High Efficiency and Stability for Photocatalytic Applications. *J. Mater. Chem. A* **2014**, *2*, 1750−1756.

(27) Guo, J. J.; Zhou, H.; Ouyang, S. X.; Kako, T.; Ye, J. H. An Ag_3PO_4/Nitridized $Sr_2Nb_2O_7$ Composite Photocatalyst with Adjustable Band Structures for Efficient Elimination of Gaseous Organic

DOI: 10.1021/acsami.5b02649
ACS Appl. Mater. Interfaces 2015, 7, 15285−15293

Pollutants under Visible Light Irradiation. *Nanoscale* **2014**, *6*, 7303−7311.
(28) Zheng, D. D.; Huang, C. J.; Wang, X. C. Post-Annealing Reinforced Hollow Carbon Nitride Nanospheres for Hydrogen Photosynthesis. *Nanoscale* **2015**, *7*, 465−470.
(29) Wang, X. C.; Blechert, S.; Antonietti, M. Polymeric Graphitic Carbon Nitride for Heterogeneous Photocatalysis. *ACS Catal.* **2012**, *2*, 1596−1606.
(30) Cui, Y. J.; Ding, Z. X.; Fu, X. Z.; Wang, X. C. Construction of Conjugated Carbon Nitride Nanoarchitectures in Solution at Low Temperatures for Photoredox Catalysis. *Angew. Chem., Int. Ed.* **2012**, *51*, 11814−11818.
(31) Zhang, G. G.; Zhang, J. S.; Zhang, M. W.; Wang, X. C. Polycondensation of Thiourea into Carbon Nitride Semiconductors as Visible Light Photocatalysts. *J. Mater. Chem.* **2012**, *22*, 8083−8091.
(32) Wang, X. C.; Maeda, K.; Thomas, A.; Takanabe, K.; Xin, G.; Carlsson, J. M.; Domen, K.; Antonietti, M. A Metal-Free Polymeric Photocatalyst for Hydrogen Production from Water under Visible Light. *Nat. Mater.* **2009**, *8*, 76−80.
(33) Gong, Y. T.; Li, M. M.; Wang, Y. Carbon Nitride in Energy Conversion and Storage: Recent Advances and Future Prospects. *ChemSusChem* **2015**, *8*, 931−946.
(34) Gong, Y. T.; Li, M. M.; Li, H. R.; Wang, Y. Graphitic Carbon Nitride Polymers: Promising Catalysts or Catalyst Supports for Heterogeneous Oxidation and Hydrogenation. *Green Chem.* **2015**, *17*, 715−736.
(35) Zhang, P. F.; Li, H. R.; Wang, Y. Post-Functionalization of Graphitic Carbon Nitride by Grafting Organic Molecule: Toward C-H Bond Oxidation Using Atmospheric Oxygen. *Chem. Commun.* **2014**, *50*, 6312−6315.
(36) Li, X. B.; Masters, A. F.; Maschmeyer, T. Photocatalytic Hydrogen Evolution from Silica-Templated Polymeric Graphitic Carbon Nitride-Is the Surface Area Important? *ChemCatChem* **2015**, *7*, 121−126.
(37) Zhao, Y.; Zhao, F.; Wang, X. P.; Xu, C. Y.; Zhang, Z. P.; Shi, G. Q.; Qu, L. T. Graphitic Carbon Nitride Nanoribbons: Graphene-Assisted Formation and Synergic Function for Highly Efficient Hydrogen Evolution. *Angew. Chem., Int. Ed.* **2014**, *53*, 13934−13939.
(38) Martin, D. J.; Qiu, K. P.; Shevlin, S. A.; Handoko, A. D.; Chen, X. W.; Guo, Z. X.; Tang, J. W. Highly Efficient Photocatalytic H_2 Evolution from Water using Visible Light and Structure-Controlled Graphitic Carbon Nitride. *Angew. Chem., Int. Ed.* **2014**, *53*, 9240−9245.
(39) Chen, J.; Shen, S. H.; Guo, P. H.; Wang, M.; Wu, P.; Wang, X. X.; Guo, L. J. In-Situ Reduction Synthesis of Nano-Sized Cu_2O Particles Modifying g-C_3N_4 for Enhanced Photocatalytic Hydrogen Production. *Appl. Catal., B* **2014**, *152*, 335−341.
(40) He, F.; Chen, G.; Yu, Y. G.; Hao, S.; Zhou, Y. S.; Zheng, Y. Facile Approach to Synthesize g-PAN/g-C_3N_4 Composites with Enhanced Photocatalytic H_2 Evolution Activity. *ACS Appl. Mater. Interfaces* **2014**, *6*, 7171−7179.
(41) Schwinghammer, K.; Mesch, M. B.; Duppel, V.; Ziegler, C.; Senker, J.; Lotsch, B. V. Crystalline Carbon Nitride Nanosheets for Improved Visible-Light Hydrogen Evolution. *J. Am. Chem. Soc.* **2014**, *136*, 1730−1733.
(42) Yang, S. B.; Gong, Y. J.; Zhang, J. S.; Zhan, L.; Ma, L. L.; Fang, Z. Y.; Vajtai, R.; Wang, X. C.; Ajayan, P. M. Exfoliated Graphitic Carbon Nitride Nanosheets as Efficient Catalysts for Hydrogen Evolution Under Visible Light. *Adv. Mater.* **2013**, *25*, 2452−2456.
(43) He, Y. M.; Zhang, L. H.; Teng, B. T.; Fan, M. H. New Application of Z-SchemeAg_3PO_4/ g-C_3N_4 Composite in Converting CO_2 to Fuel. *Environ. Sci. Technol.* **2015**, *49*, 649−656.
(44) Katsumata, H.; Sakai, T.; Suzuki, T.; Kaneco, S. Highly Efficient Photocatalytic Activity of g-C_3N_4/Ag_3PO_4 Hybrid Photocatalysts through Z-Scheme Photocatalytic Mechanism under Visible Light. *Ind. Eng. Chem. Res.* **2014**, *53*, 8018−8025.
(45) Chen, X. X.; Huang, X. T.; Yi, Z. G. Enhanced Ethylene Photodegradation Performance of g-C_3N_4-Ag_3PO_4 Composites with Direct Z-Scheme Configuration. *Chem. - Eur. J.* **2014**, *20*, 17590−17596.
(46) Kumar, S.; Surendar, T.; Baruah, A.; Shanker, V. Synthesis of a Novel and Stable g-C_3N_4-Ag_3PO_4 Hybrid Nanocomposite Photocatalyst and Study of the Photocatalytic Activity under Visible Light Irradiation. *J. Mater. Chem. A* **2013**, *1*, 5333−5340.
(47) Yang, X. F.; Tang, H.; Xu, J. S.; Antonietti, M.; Shalom, M. Silver Phosphate/Graphitic Carbon Nitride as an Efficient Photocatalytic Tandem Syetem for Oxygen Evolution. *ChemSusChem* **2015**, *8*, 1350−1358.

DOI: 10.1021/acsami.5b02649
ACS Appl. Mater. Interfaces 2015, 7, 15285−15293